

Optimizing Solid Microneedle Design: A Comprehensive ML-Augmented DOE Approach

Ahmed Choukri Abdullah, Erfan Ahmadinejad, and Savas Tasoglu*



Cite This: *ACS Meas. Sci. Au* 2024, 4, 504–514



Read Online

ACCESS |



Metrics & More



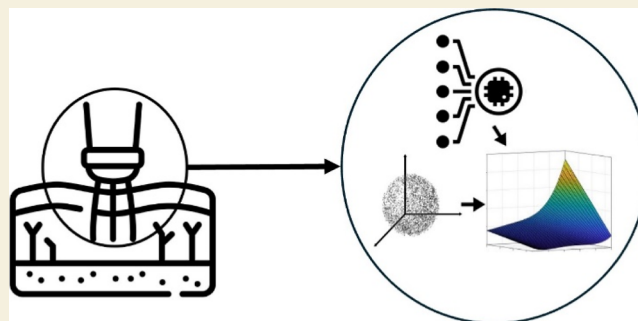
Article Recommendations



Supporting Information

ABSTRACT: Microneedles (MNs), that is, a matrix of micro-meter-scale needles, have diverse applications in drug delivery, skincare therapy, and health monitoring. MNs offer a minimally invasive alternative to hypodermic needles, characterized by rapid and painless procedures, cost-effective fabrication methods, and reduced tissue damage. This study explores four MN designs, cone-shaped, tapered cone-shaped, pyramidal with a square base, and pyramidal with a triangular-shaped base, and their optimization based on predefined criteria. The workflow encompasses three loading conditions: compressive load during insertion, critical buckling load, and bending loading resulting from incorrect insertion. Geometric parameters such as base radius/width, tip radius/width, height, and tapered angle tip influence the output criteria, namely, total deformation, critical buckling loads, factor of safety (FOS), and bending stress. The comprehensive framework employing a design of experiment approach within the ANSYS workbench toolbox establishes a mathematical model and a response surface fitting model. The resulting regression model, sensitivity chart, and response curve are used to create a multiobjective optimization problem that helps achieve an optimized MN geometrical design across the introduced four shapes, integrating machine learning (ML) techniques. This study contributes valuable insights into a potential ML-augmented optimization framework for MNs via needle designs to stay durable for various physiologically relevant conditions.

KEYWORDS: microneedles (MNs), machine learning (ML), optimization, design of experiment (DOE), finite element analysis (FEA)



INTRODUCTION

A micron-scale needle, also known as a microneedle (MN),^{1,2} is a minimally invasive needle used for injection,^{3,4} dermal and transdermal delivery of drugs,^{5–8} biological substances,⁹ skin care therapy,^{10,11} and monitoring glucose levels¹⁰ through extraction of a special fluid known as interstitial fluid (ISF).^{5,12} MNs have been a substitute of hypodermic needles due to their rapid painless procedure,^{11,13–15} affordable fabrication methods,⁹ reduced tissue rupturing, and self-handle and compact administration.¹¹ Their capabilities of penetrating the skin layer with the goal of transferring proteins,⁹ DNA,^{9,14} and vaccines^{9,14,16,17} in the most efficient and minimally invasive manner make MNs a promising technology for various medical applications.^{11,18,19} Moreover, researchers show that MNs can be incorporated with diagnostic capabilities to assess diseases based on painless experience and monitoring the health condition by means of invasive and noninvasive methods.^{3,4,6,11} Other applications have been developed for cosmetic implementation in hair implants and growth.¹¹ The controlled usage through MNs enhances the therapeutic efficacy while minimizing potential side effects associated with traditional hypodermic needles.⁴ Unfortunately, MNs can break during insertion/withdrawal into/from the skin.²⁰

MNs exhibits a diverse range of classification based on their functions such as solid, hollow, dissolvable, and coated MNs.^{5,6,21} A variety of materials have been used for fabrication using silicon, stainless steel, polymers, and others.^{2,4,22,23} First, the solid MNs also known as “poke with patch” have a solid structure without any channels or cavities inside.^{2,5,15,24} They are typically designed to penetrate the outmost layer of the skin, stratum corneum (SC),^{5,6,21,24} to aid the drug transport deep into the dermis layer by creating a pathway to enhance the absorption and delivery of substances.⁵ Unlike traditional needles, the solid MNs are adequate for vaccine delivery as they maintains their effectiveness over an extended period and trigger a stronger antibody response.^{2,3,21} They are flexible in design, are easy to fabricate, and have great mechanical properties.²³ They are used for pretreatment of the skin by creating pores for drug delivery.²³ The second class of MNs is

Received: April 23, 2024

Revised: July 24, 2024

Accepted: July 24, 2024

Published: August 6, 2024



the hollow MNs, referred to as “poke and flow”, primarily utilized for vaccination or storing drug fluids within their empty core,^{15,21,25} hence earning the name. They allow the passage of various biological substances, drugs, and some cosmetic formulations directly into the skin through its central channel.²¹ Compared to solid MN, the hollow MNs can handle a substantial quantity of fluids, giving them the ability to deliver these substances into the dermis site.^{21,26} Furthermore, hollow MNs are ideal for controlling the quantity and flow rate of these fluids, determining when they are released over time.^{2,21} On the downside, they are susceptible to breakage and cracks due to their weak mechanical strength compared to that of the solid MN and may suffer from blockage and clogs by skin during insertion handling.^{12,22} To overcome these barriers, the hollow MNs are being designed as a semisolid tip to endure the insertion strength.^{12,27} Meanwhile, implementing a side hole at the tip minimizes resistance to liquid flows while maximizing the surface area exposed to the skin.^{12,28,29} The coated MN contains a desired substances coated around the solid tip, “coat and poke”.^{15,21} The purpose of this type is to facilitate the release of the substances upon insertion into the skin, providing an accurate, efficient, and rapid delivery method. These substances include small molecules, DNA, proteins, peptides, and viruses.^{15,21,30,31} The site of delivery is not only limited to skin, and they can be used for delivery into the eye,^{30,32–34} vascular tissue,^{30,35,36} and oral cavity.^{30,37,38} However, due to the design, less quantity of drugs can be carried.²¹ The last type of MN is the dissolving MNs, which are made from materials that dissolve upon insertion into the skin.^{3,21} They are commonly used for the controlled release of drugs or bioactive compounds into the skin. They are referred to as “poke-and-release”, which provides instant sustained delivery to the site of insertion of macromolecules.^{3,39} They are easily administered for drug delivery purposes as the tip is loaded using a casting method.^{21,26} During the infusion of dissolvable MNs into the skin, the drug coating is released and diffuses freely to the targeted site. However, a drawback arises from the complete injection of the MNs into the layer, which might pose a challenge to achieve.⁴⁰

MNs are similarly classified according to their different shape base geometry such as triangular, circular, square, and hexagonal.²² These can be fabricated in any type of MN discussed earlier. Each shape and type is designed efficiently for a specific purpose and can perform well in that specific application.⁴¹ MNs are formulated in numerous sizes depending on the type and material used. Lengthier and thicker needles that can pierce deeper into the dermis layer (around 1500 μm) may provoke pain and damage the nerves. Usually, MNs span the range of 150–1500 μm in length,^{2,19} with 250 μm width and approximately 1–25 μm thickness at the tip,^{2,42} which can be cylindrical, triangular, pointed, or any other polygon shape.^{11,43} Additionally, it has been illustrated by Nalluri et al. that for the best cell activation, the height should not exceed 1.5 mm.^{6,44} Some studies have indicated that the tip radius influences both the mechanical properties and the pain induction associated with MNs. A recorded tip radius ranging from 1 to 25 μm has been associated with a painless insertion procedure, showing an inverse relationship with a higher range up to 38 μm .^{45,46} Additionally, the force needed to puncture the skin correlates with tip sharpness, thereby influencing the perception of pain. Some outlined the design of semisolid hollow conical MNs with a height of 600 μm , a base diameter of 200 μm , and less than 20 μm tip diameter for extraction and delivery application.^{12,47} For lengths above 1000 μm , the MN tends to produce frictional

resistance, providing little pain experience, but it offers enhanced penetration during insertion compared to short MNs.^{12,48,49}

Several studies provided information about the force required for insertion, which ranges between 30 and 70 mN depending on different MN geometries and materials.⁶ Another study reported the required force to go through the SC (thickness of 20 μm) is 0.3 N using a silicon MN.⁵⁰ Interestingly, Davis, Landis, Adams, Allen, and Prausnitz⁵¹ formulated a linear fit through experimental measurements and theoretical modeling as a function of the tip cross-sectional area of the needle.^{6,10,51} The MN was generalized for a hollow structure that has a tapered tip radius ranging between 30 and 80 μm and a wall thickness of 5–58 μm with a constant height of 720 μm using a metal material. The insertion force varied between 0.08 and 3.04 N.^{10,51} It is worth noting that due to the structure of the MN, precautions measurements should be ensured so as to not fracture or bend during the insertion procedure.¹⁰ Thus, the insertion force is a vital parameter to ensure safety design.¹⁰ Additionally, it is essential for the MNs to hold down substantial insertion forces without experiencing deformation or causing pain.¹² Another way to quantify the insertion force into the skin is to overcome the elastic property of the skin layer.¹⁰ Typically, the SC layer has a modulus of 3.18 MPa, which drops postpuncture to an elasticity value in the dermis layer, reaching 1.6 MPa.^{9,12,51–53} This pressure puncture defines the resistance force correlated to the projected cross-section area of the tip.^{16,20} A dissolving MN patch (pyramidal geometry) has been designed to have sufficient mechanical strength to be inserted without breakage and buckling.^{10,13}

Numerical simulation of MNs has been widely used in the recent years.^{22,54,55} An earlier study investigated the simulation of a MN array into the skin using LS-DYNA (ANSYS).⁵⁶ Their simulation consisted of four types of geometry (cone, tapered-cone, beveled-tip, and pyramidal with a square base) for varied sizes of the model using polymer polylactic acid (PLA). The purpose of that study was to observe the insertion force distributed along the MN array into the skin model.⁵⁶ Different loading conditions on a single MN has been observed through finite element analysis (FEA) for conical and pyramidal shapes.⁵⁷ A compressive force is applied perpendicular to the cross-sectional area of the tip using a fixed base. This axial force induces buckling and deformation in the tip, with the buckling force dependent on the geometrical lengths and mechanical properties of the material.⁵⁷ Mishra et al. has used finite element method (FEM) approximation to rigorously show that the von Mises stress increases as an exponential function of the inner radius of the hollow MN. It was quantified for a hollow SU-8 MN array designed using direct laser writing (DLW) that is strong enough to withstand the human skin elasticity.²⁰ Critical buckling modeled equations of simple square pyramidal and cylindrical cone have been formulated by Smith for a fixed base MN.⁵⁸ The formulas are approximations based on the analytical energy approach method. Simulation results for conical and pyramidal designs for different materials have been used for comparison by applying 10 kPa force on a single MN.⁵² They concluded that the design combination along with the material type PVA was the choice that can withstand stress and deformation to successfully penetrate the skin. One study has observed different material groups including metal, ceramic, polymer, and glass, where a structural analysis through COMSOL Multiphysics has been performed to analyze the influence of several forces, i.e., axial, buckling, and bending forces into the skin.⁵⁹ PLA and polycarbonate underwent

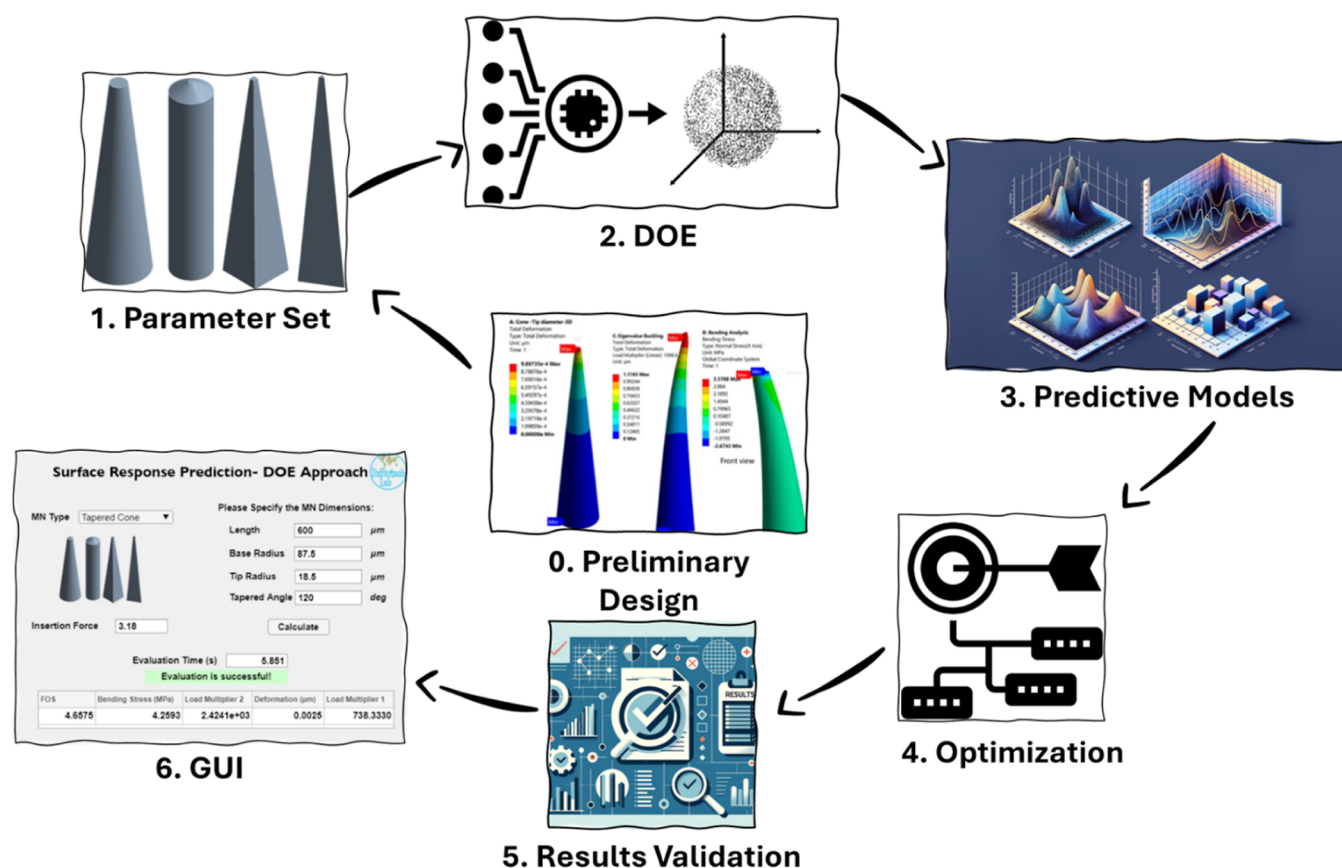


Figure 1. Flowchart illustrates the analysis and optimization process for four distinct MN designs; cone and tapered shaped and square and pyramidal base shaped. Step 0 involved subjecting the MNs to three loading conditions: compressive load during insertion, critical buckling load, and bending loading due to wrong insertion. Step 1 involved transferring the model into a set of input–output links such that a matrix correlation can be built, representing the relationship of what parameters can affect these analyses. Step 2 included the sampling the design space of the data using a sampling algorithm for the DOE. Step 3 provided a training procedure of DOE data to be fitted into the regression models. The regression model was able to produce the response surface curve, the sensitivity chart, and the prediction models such that no further FEA runs are needed. According to the obtained results in step 3, optimization through RSO was executed using multiobjective algorithms, step 4. The geometrical results of the optimization were validated using the computation model of FEA, step 5. Finally, a GUI was created to serve as a user-friendly mode for testing and exploring new design patterns, step 6.

buckling and were not considered as the choice of material. However, silicon carbide was selected among all the 10 presented materials for withstanding the loading conditions specified.⁵⁹

This study explores four distinct MN designs: cone-shaped, tapered cone-shaped, and pyramidal with square and triangular shaped MNs, in which they will be optimized based on predefined criteria. Figure 1 summarizes the workflow of our study. The MNs will undergo three different loading conditions: compressive load during insertion, critical buckling load, and bending loading resulting from incorrect insertion (step 0). These prerequisites are constrained according to a set of predefined values, and a minimax multiobjective optimization problem is addressed to be satisfied later. In accordance with the geometric model, input parameters consist of geometric features such as base radius, tip radius, height, angle tip, and others. Meanwhile, the output parameters will be determined by obtaining criteria results, including total deformation at the tip, critical buckling loads, factor of safety (FOS), and bending stress (step 1). Subsequently, a framework was developed using the design of experiment (DOE) approach, which is part of the ANSYS workbench suite (step 2). This framework systematically links the inputs and outputs as a mathematical model through the available response surface fitting models in the

ANSYS workbench, including machine learning (ML) algorithms for regression fitting. By obtaining the complete regression model that represents the coupled equation, the framework also provides a sensitivity chart of the inputs and a response curve (step 3). Finally, the optimization problem is preset to search using the multiobjective algorithms through the response surface to acquire an optimized MN geometrical design across four different shapes (step 4). Most importantly, the geometrical results are validated using the corrected FEA computational model (step 5). As a concluding step, a graphical user interface (GUI) is created to serve as a user-friendly module (step 6).

METHODS AND MATERIALS

Four distinctive silicon MN designs were selected for this study. For demonstration purposes, the cone shape is considered in the current work. The dimensions of the designs have been restricted as shown in Table 1. One difficulty we suffered during the FEA modeling was from the singularities at the sharp tip, which would create artificially infinite stress. Therefore, all of the designs were modified to have a flat surface, which was expressed as a parameter (tip diameter/width) later. The primary objective in choosing these designs was to assess their fabrication,

Table 1. Parametric Design Ranges for the MN Dimensions

parameter	range
base diameter/width (μm)	[50, 300]
tip diameter/width (μm)	[10, 40]
length (μm)	[200, 1000]
tapered angle (deg)	[105, 135]

performance testing, and failure analysis in relation to the application of MNs puncturing into skin layers. Data were collected for the insertion of a MN into the skin as a function of the interfacial area and resulted in a line fitting as⁵¹

$$F_i = 0.00019A_f - 0.66$$

where F_i and A_f are the insertion force (N) and full cross-sectional area of the needle (μm^2), respectively. Yet, this was only valid within a certain range of interfacial area. The most accurate way to quantify the insertion force was to consider overcoming the elasticity layer of SC as 3.18 MPa. A set of criteria was proposed in this study: (1) static analysis, (2) buckling analysis, and (3) bending analysis. The MNs were subjected to these failures, which provide us a goal to assess and optimize these designs accordingly. A lateral deformation will be conducted to ensure that the MN maintains its intended shape and dimension intact, static analysis. The critical buckling load was computed and the mode shape was observed, which provided at what force the MN can potentially buckle through the buckling analysis. In the case of incorrect insertion, bending behavior of the MN was checked where the FOS and bending stress are computed, bending analysis. The boundary conditions (BCs) for MN insertion were replicated to closely resemble real conditions in ANSYS Mechanical. A uniform distribution of pressure force of 3.18 MPa is applied at the tip and a fixed support at the base of the MN. Some of the preliminary results of deformation, buckling, and bending analyses can be shown in Figure 2 for length 400 μm , base diameter 80 μm , and tip

diameter 10 μm as a reference model. The load multiplier represents the multiplying factor with respect to the applied load on the MN ($3.18/A_f$). Thus, the respected critical buckling force for the first two modes shown are 0.27 and 0.85 N, respectively. As mentioned earlier, the insertion force varies within the range of few newtons. Hence, there is no discrepancy between the literature and the current FEA done here. Additionally, the predefined yield stress was set to 173.2 MPa for silicon, and a FOS of 12 was measured in the reference design.

The proposed approach in this work was to predict and optimize the MN designs based on specific defined criteria, i.e., minimizing deformation and bending stress and avoiding critical buckling load through maximizing the load multipliers with a constrained above 1.5 FOS limit. This was done through applying the DesignXplorer toolbox in ANSYS through the DOE approach, then predicting the nature behavior of the nonlinear models, and finally using a custom multiobjective optimization algorithm to propose the best design combination.

DOE for the Predictive Model

The DOE was set to generate 200 design points using the latin hypercube sampling (LHS) technique for each MN design while obeying the restrictions set earlier. LHS creates sampling points that sparse the design space for exploring the behavior of the model, where it provides a good coverage of the parameter space, reducing the number of simulations needed to correctly model the problem. For each input parameter, random samples are extracted from an interval, ensuring that an instance was picked up at least once, providing more sparse and robust sampling, unlike Gaussian or random sampling algorithms.

To accurately represent the relationship between the input parameters and the response variables, a predictive ML model was constructed by using the Kriging method, a response surface approach facilitated by the ANSYS toolbox. Kriging, also known as Gaussian process regression (GPR), is a powerful interpolation technique that can capture deterministic trends

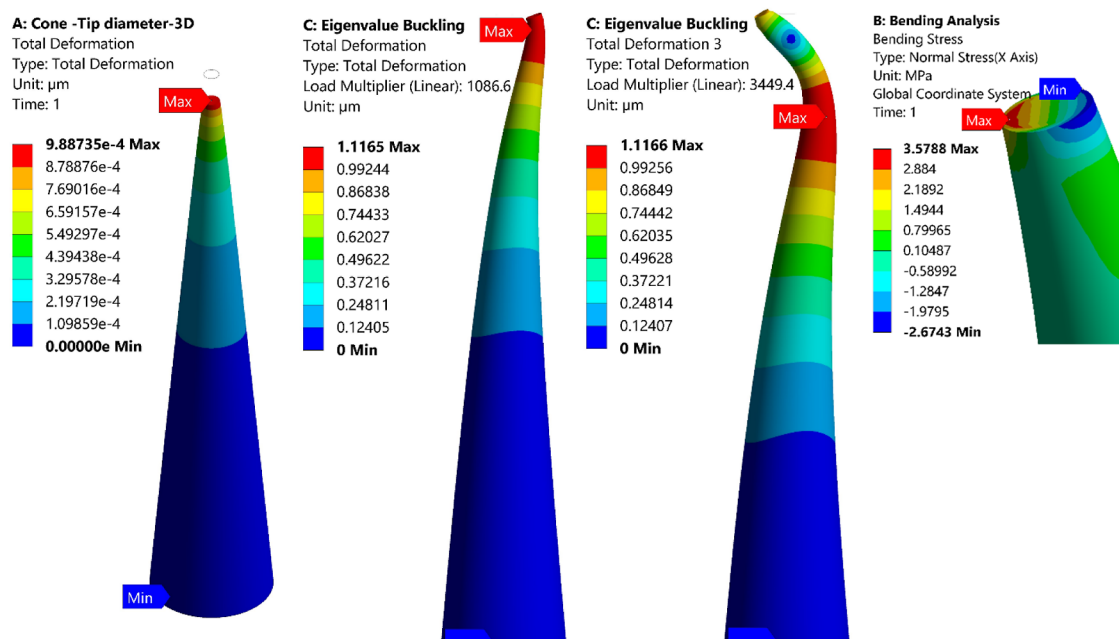


Figure 2. Preliminary analysis: deformation occurring during MN insertion, which shows the maximum located at the tip of the insertion. Buckling analysis, which provided the critical buckling load and the buckling mode, provided that for a certain force, buckling can be observed in the MN. Finally, bending analysis serving the special case of wrong insertion, causing a deflection bend at the MN body and tip, producing large bending stress.

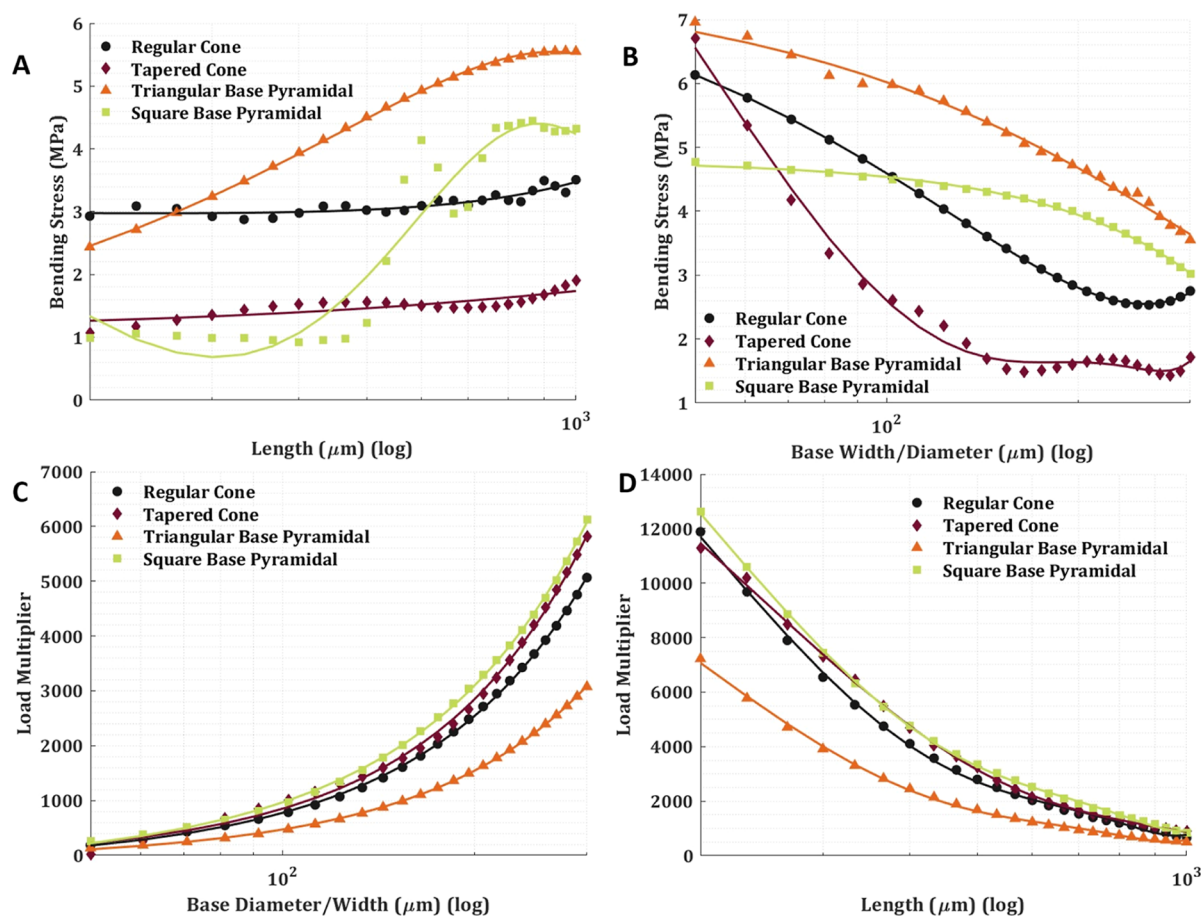


Figure 3. Two-dimensional fitting models trained using ML GPR for all the different MN designs. Each subplot illustrates the relationship between specific parameters and either normal stress or load multiplier for the four MN designs. (A) Normal stress as a function of length. The model predicted an increase in stress with the increase in the length. (B) Normal stress decreases as the base diameter/width is decreased. (C) The load multiplier modeled increased proportionally with the increase in the base diameter/width; meanwhile, (D) the load multiplier exponentially decreased with the length. Note that the obtained plots were plotted using semilog for the x -axis.

in the data, especially for small data sets, while also accounting for correlations between different input combinations. It assumes that the process is of a Gaussian random field, making it suitable for capturing the variability in the response variables within the design space. Moreover, the method includes reliable estimates of the uncertainty associated with the predictions to be made, making it an excellent choice for the models that require optimization and sensitivity analysis. Hyperparameter tuning for the Kriging algorithm was involved, ensuring maximum accuracy in predicting the response variables and generalizing unseen data points within the parameters' space. The associated regression model prediction and goodness of fit are provided in Figures 3 and 4, respectively. The root mean square error (RMSE) scores for the regression model have been reported, indicating the precision of the model's predictions into how well the regression model aligns with actual data. The performance shows that the deformation and load multiplier are more closely fitted to the observed data. On the other hand, the bending normal stress and FOS parameters scored lower accuracy, which biased the results in the prediction and optimization models. Yet, the bending normal stress is in the order of expectancy of the model and does not affect the overall of the model performance, as reported in the Optimization Models Using Response Surface Optimization section.

Once the model was satisfied in terms of accuracy, enough DOE data points are set to build up the response surface plots,

serving as visual representation for prediction and analysis, Figure 5. The surface plots provided help to make further predictions without the need for simulating new model designs, ensuring that the unseen trained data fall into the surface region. Some of the input parameters vary linearly, such as the deformation produced with respect to the tip and length. However, with the base, the deformation has an exponential growth behavior, showing its important design role for MN insertion. Additionally, spider (radar) plots were provided for each MN design, Figure 6. The key parameter significantly influencing the response parameters was the length. For instance, the length exhibited a strong inverse correlation with buckling analysis for all designs and a direct correlation with bending analysis. The base was proceeded with considering its importance on total deformation and the formation of stresses on the MN, hence jeopardizing the FOS. Therefore, a safe optimal design may be chosen considering the priority of these two design parameters. However, the taper angle had no dependence on the response parameters for tapered design. Other sensitivity information can be read from the radar plots.

Optimization Models Using Response Surface Optimization

Unlike direct optimization that involves directly optimizing the objective function based on given metrics iteratively, which can be computationally expensive, response surface optimization

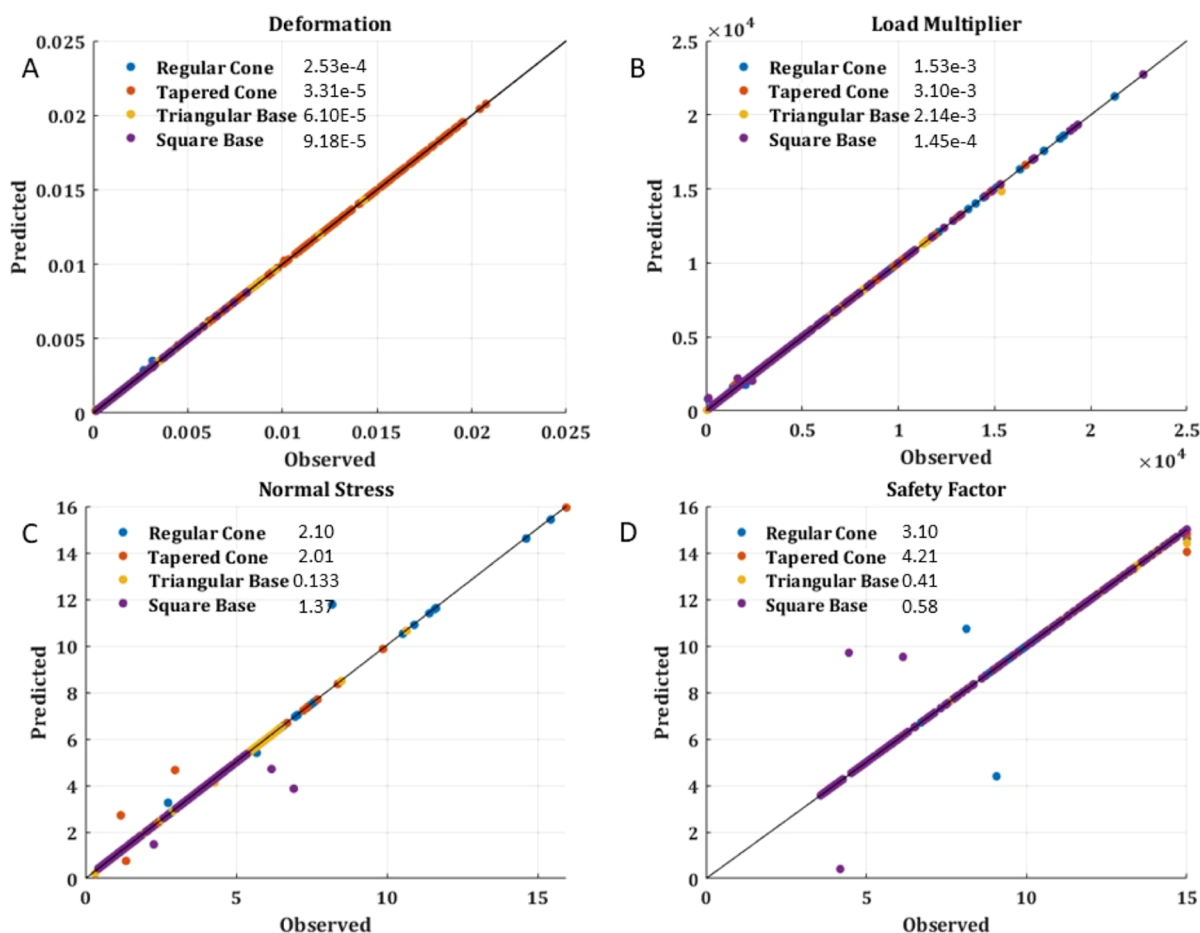


Figure 4. Goodness of fit for the predictive model reported with RMSE scores. The predictive model was able to accurately capture (A) deformation and (B) load multipliers, while (C) bending normal stress exhibited some deviation. It has been observed that the (D) FOS consistently remains above the threshold score of 15. However, the model cannot fully predict the FOS. Thus, it was placed as an optimization constraint.

(RSO) can be used for approximating the behavior of the objective function based on building a surrogate model, the response surface, to guide the optimization process in an exploration approach. Since the optimization algorithm interacts with the response surface model rather than the actual objective function, RSO is considered computationally more efficient to use for a long complex model. It involves balancing between exploring the design space to refine the surrogate model and exploiting the current space to efficiently identify an optimal solution efficiently. However, the accuracy of RSO is of the order (if not more) to the surrogate model's accuracy; hence, a more accurate surrogate model is desired.

The RSO algorithm was set to the screening algorithm to identify the optimal set of input parameters that would yield the desired response variable for a MN design. As mentioned earlier, the multiobjective function corresponds to the specific performance defined as minimizing the total deformation at the tip and the bending stress and maximizing the critical buckling loads while staying within the FOS limitation. The screening method can handle a large number of input parameters, five independent variables, by computing a subset of input parameters together and checking if they meet the required problem formulated. We were able to achieve top three candidate points with only the best candidate points reported in Tables 2–5 along with the validated FEA models in ANSYS. The algorithm iteratively ran for 3000 evaluations based on the optimal selection parameters; the results illustrated good consistency with the validated FEA

model, as discussed earlier in the goodness of fit results, which was controlled by the accuracy of the model fit. Both the deformation and load multiplier were scored very close to the verified FEA model along with the normal stress. However, the FOS has not been accurately captured since the FEA model cannot compute a score higher than 15. Hence, the FOS was retained as a limitation constraint and not for prediction purposes. The indirect optimization problem via screening, as described above, has a simulation time of less than a minute. Unlike the direct optimization, which can take many days to find the optimal solution. However, the initial step of generating the DOE data points required approximately 1 to 2 days. These simulation times reflect the computational efficiency of our approach, balancing thorough parameter exploration with practical time constraints. Finally, the performance of the tapered cone design was reasonable for deformation and stress analysis but not accurate for buckling analysis with 20% error and, therefore, cannot be reliable in finding the correct critical buckling load.

GRAPHICAL USER INTERFACE

A GUI has been designed for this study, which served as a user-friendly platform for predicting the common MN designs, as shown in Figure 7. The interface allows users to input the design parameters, length, base, tip, and taper angle, if available, and then predicts the response parameters based on the surface response kriging algorithm built in. The GUI clearly established

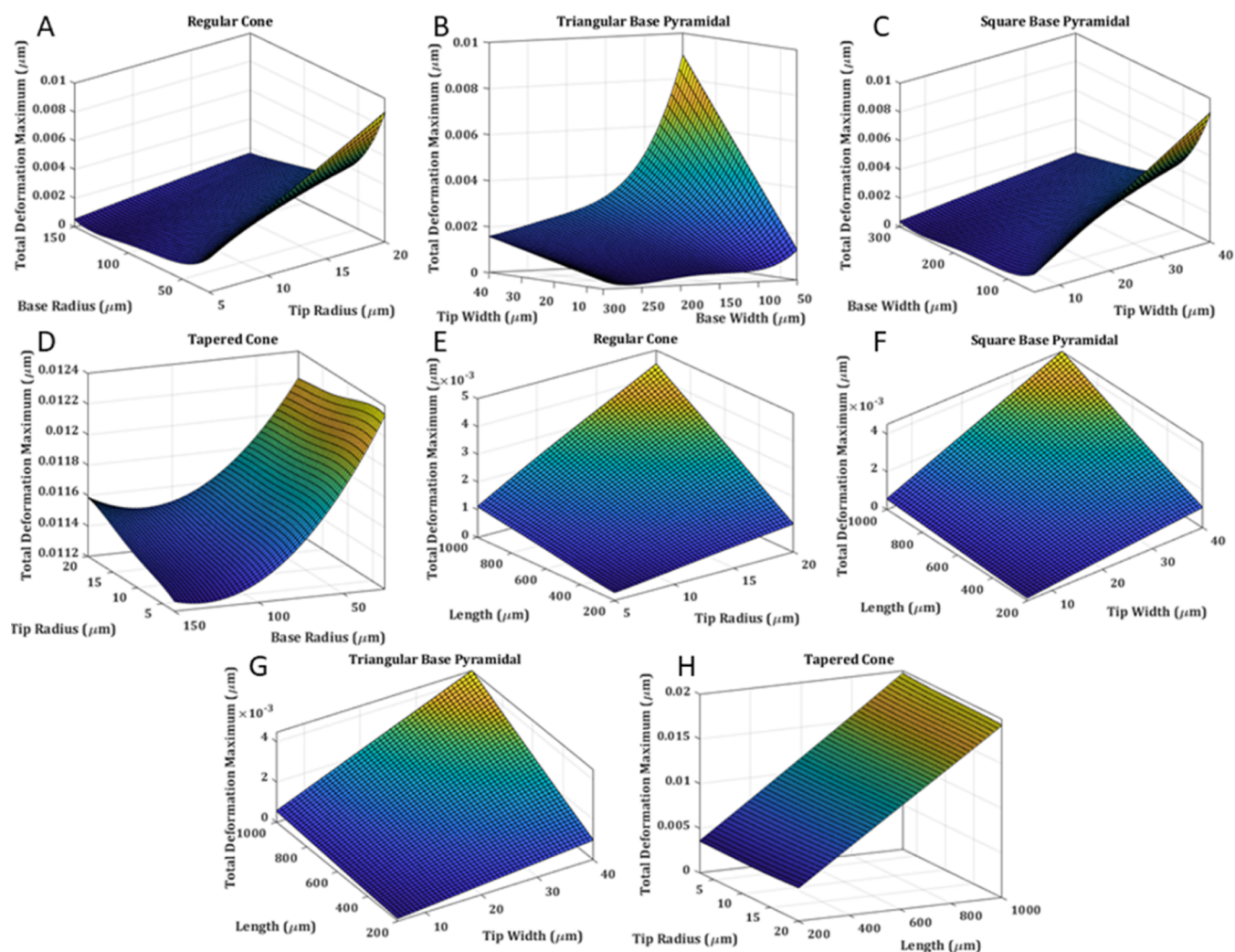


Figure 5. Surface response representing the relation among the base, tip, length, and deformation variables. The surface response plots illustrate the relationship between various parameters and total deformation for different MN designs. Subfigures (A–D) depict the combination of base and tip radius/width vs total deformation for all MN designs, while subfigures (E–H) show the relationship between length and tip radius/width vs total deformation. The plots can be used to predict the expected total deformation occurring during insertion for any two-dimensional parameter given.

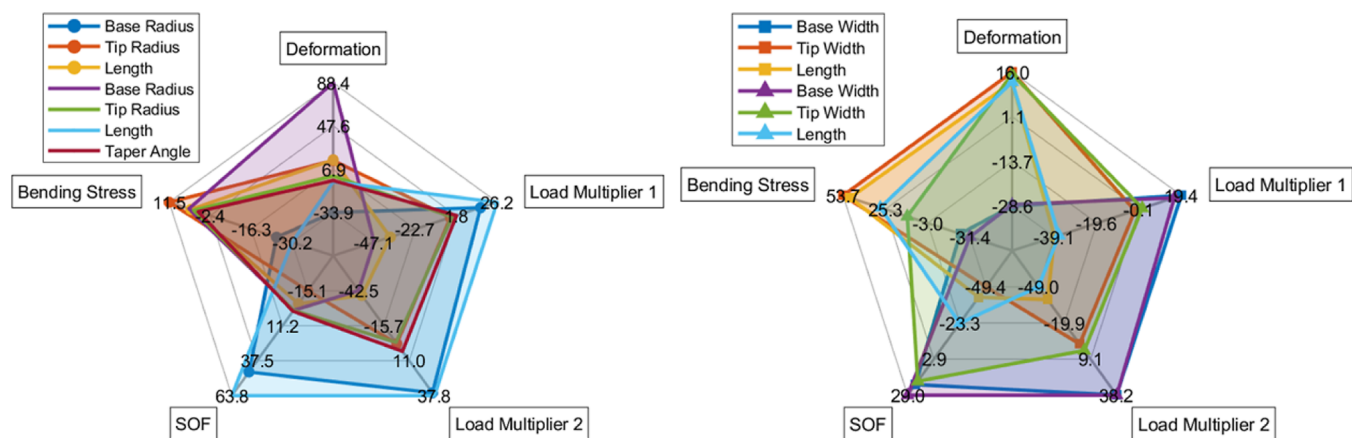


Figure 6. Sensitivity analysis for MN designs for the regular and tapered cone and square and triangular base. The left radar plot contains the regular and tapered cone combined, while the right radar plot contains the square and triangular pyramidal base MNs.

a link between input parameters and the expected response variables, providing users with a reliable predictive model without the need of using FEA software, offering a low computation cost solution. Additionally, insertion force of MN

has been supported to explore different possible scenarios for any MN designs.

Table 2. Obtained Optimization Results Verified the Actual FEA Model for Regular Cone Design

regular cone		
parameter	candidate point	FEA (verified)
base diameter (μm)	311.64	
tip diameter (μm)	10	
length (μm)	200	
FOS	15.32	15
load multiplier 1	20.70×10^3	21.95×10^3
load multiplier 2	28.74×10^3	32.12×10^3
total deformation maximum (μm)	1.88×10^{-4}	2.32×10^{-4}
normal stress maximum (MPa)	1.01	1.15

Table 3. Obtained Optimization Results Verified the Actual FEA Model for Square Base Pyramidal Design

square base pyramidal		
parameter	candidate point	FEA (verified)
base width (μm)	300	
tip width (μm)	10	
length (μm)	200	
FOS	17.57	15
load multiplier 1	30.30×10^3	31.24×10^3
load multiplier 2	36.11×10^3	38.71×10^3
total deformation maximum (μm)	1.23×10^{-4}	1.14×10^{-4}
normal stress maximum (MPa)	0.30	0.28

Table 4. Obtained Optimization Results Verified the Actual FEA Model for Triangular Base Pyramidal Design

triangular base pyramidal		
parameter	candidate point	FEA (verified)
base width (μm)	243.83	
tip width (μm)	10	
length (μm)	200	
SOF	15.54	15
load multiplier 1	14.78×10^3	14.81×10^3
load multiplier 2	23.39×10^3	25.28×10^3
total deformation maximum (μm)	1.12×10^{-4}	1.03×10^{-4}
normal stress maximum (MPa)	0.49	0.35

Table 5. Obtained Optimization Results Verified the Actual FEA Model for Tapered Cone Design

tapered cone		
parameter	candidate point	FEA (verified)
base diameter (μm)	131.52	
tip diameter (μm)	5.97	
length (μm)	200	
tapered angle (deg)	135	
safety factor minimum	15.48	15
load multiplier 1	9.14×10^3	11.65×10^3
load multiplier 2	14.10×10^3	18.57×10^3
total deformation maximum (μm)	3.22×10^{-3}	3.39×10^{-3}
normal stress maximum (MPa)	0.10	1.25

Future Perspective and Limitations

The MNs described in this work reflect the ability of a MN to penetrate through the elasticity layers of the skin. While the framework does not directly measure the mechanical properties of the MNs, the FOS proposed provides an indication of the safety during insertion. Therefore, the work primarily considers

the force magnitude and successful skin penetration. Additionally, other factors, such as the fabrication technique and biocompatibility, play a crucial role in determining the final shape of the MNs.

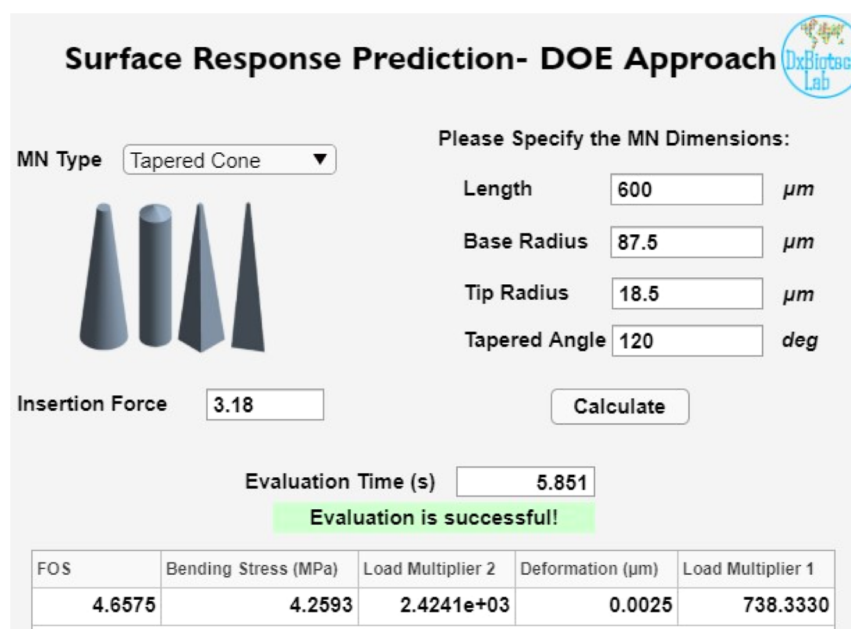
Different fabrication techniques impact the geometric precision of the MNs. Common methods, such as lithography, molding, and 3D printing, can be utilized. Each technique has its own set of advantages and limitations. For instance, lithography allows for high-precision fabrication, easy to control features through etching, and fast speed productivity but is highly expensive and requires harsh processing conditions compared to other methods.⁶⁰ On the other hand, molding is more cost-effective and suitable for mass production, yet it compromises on precision.⁶¹ 3D-printed MNs offer enhanced capabilities for customization, rapid fabrication, and cost-effectiveness.^{62–64} The 3D printing techniques are based on fully automated fabrication, which solves many issues related to producing diverse structures with topological surfaces (e.g., tip profile) unlike the traditional lithography methods. Nevertheless, 3D printing technologies are limited to their material availability.^{60,62}

Moreover, the biocompatibility of the materials used are essential for ensuring noninflammatory or allergic response.⁶⁵ In our work, the silicon material is assumed to be a very biocompatible and biodegradable material, which has been verified by an earlier work.⁶⁶ Moreover, silicon MNs were coated with titanium and gold sputtering, which increases the mechanical strength⁶⁷ and provides a better thermal and chemical stability.⁴ The choice of material directly influences the MNs' ability to withstand insertion forces without breaking and to maintain their structural integrity during and after insertion.

The proposed designs served the general cases for skin types and are not patient specific. Accordingly, future research can target a specific group of patients with a new skin model and customized MNs that serve the purpose of needle puncturing. On the framework point of view, new ML and deep learning (DL) algorithms can be fitted and used to find patterns and relationships between geometric features of MNs and their responses. Other DOE algorithms can be integrated to replace the current algorithm, which can provide better results. Such algorithms are not limited to a genetic algorithm combined with simulated annealing, which is a derivative-free based optimization method. Sparse grid and Box–Behnken design samplings are good options to avoid update failures during sampling due to extreme parameter values located at the corner. Specifically, the sparse grid can refine the DOE sampling in the direction needed to have fewer design points and can effectively handle discontinuities. However, Box–Behnken is limited to 12 input parameters. In other words, those algorithms can be an alternative option for the LHS.

CONCLUSIONS

In this study, we present a comprehensive approach for predicting and optimizing common MN designs based on specific criteria, including minimizing deformation and bending stress while avoiding critical buckling loads by maximizing within a constraint, FOS limit. The methodology involved a DOE approach that incorporates advanced optimization techniques to ensure efficiency and accuracy in the design exploration process. The employed LHS provided a sparse distribution by generating 200 design points for each MN design, offering a comprehensive exploration of parameter



Surface Response Prediction- DOE Approach

MN Type: Tapered Cone

Please Specify the MN Dimensions:

Length: 600 μm

Base Radius: 87.5 μm

Tip Radius: 18.5 μm

Tapered Angle: 120 deg

Insertion Force: 3.18

Calculate

Evaluation Time (s): 5.851

Evaluation is successful!

FOS	Bending Stress (MPa)	Load Multiplier 2	Deformation (μm)	Load Multiplier 1
4.6575	4.2593	2.4241e+03	0.0025	738.3330

Figure 7. GUI that has the capability to apply the surface response prediction for different common MN designs. The user may enter different MN dimensions based on the chosen design and specify the insertion force applied. Then, using the built-in trained model, the user can receive the feedback on the predicted values for the response parameters.

combinations while reducing the number of simulations needed for accurate modeling and avoiding nonlinear optimization methods. The input parameters and the response variables were linked using the augmented ML algorithm and the Kriging method, which captured the complex relationship and accounted for the correlation between different input combinations. The obtained results provided a good predictive model with low error values that gave a reliable estimate of uncertainty associated with predictions. Finally, the results obtained from the RSO screening method satisfied our defined set of criteria by identifying the optimal design input parameters. The candidate points were then validated using the FEA models, providing a very small deviation from the actual results. Our integration of predictive modeling to RSO presents an application and foundation for low computational cost and complex models to be accounted for. Additional advancements are required by using different sampling and optimization algorithms for specific applications.

■ ASSOCIATED CONTENT

SI Supporting Information

The Supporting Information is available free of charge at <https://pubs.acs.org/doi/10.1021/acsmesuresciau.4c00021>.

Still image from the video demonstrating the functionality of the GUI (PDF)

Video demonstrating the functionality of the GUI (MP4)

■ AUTHOR INFORMATION

Corresponding Author

Savas Tasoglu – Department of Mechanical Engineering, Koç University, Istanbul 34450, Türkiye; Koc University Is Bank Artificial Intelligence Lab (KUIS AILab), Koç University, Istanbul 34450, Türkiye; Koç University Translational Medicine Research Center (KUTTAM), Koç University, Istanbul 34450, Turkey; Boğaziçi Institute of Biomedical Engineering, Boğaziçi University, Istanbul 34684, Türkiye;

Koç University Arçelik Research Center for Creative Industries (KUAR), Koç University, Istanbul 34450, Türkiye;

ORCID: orcid.org/0000-0003-4604-217X; Email: stasoglu@ku.edu.tr

Authors

Ahmed Choukri Abdullah – Department of Mechanical Engineering, Koç University, Istanbul 34450, Türkiye; ORCID: orcid.org/0000-0003-2313-184X

Erfan Ahmadinejad – Department of Mechanical Engineering, Koç University, Istanbul 34450, Türkiye; ORCID: orcid.org/0009-0004-8317-0909

Complete contact information is available at: <https://pubs.acs.org/10.1021/acsmesuresciau.4c00021>

Author Contributions

CRedit: **Ahmed Choukri Abdullah** conceptualization, methodology, software, validation, visualization, writing-original draft; **Erfan Ahmadinejad** conceptualization, methodology, software, validation, visualization, writing-original draft; **Savas Tasoglu** conceptualization, funding acquisition, investigation, project administration, supervision, writing-review & editing.

Notes

The authors declare no competing financial interest.

■ ACKNOWLEDGMENTS

S.T. acknowledges the TÜBİTAK 2232 International Fellowship for Outstanding Researchers award (118C391), TÜBİTAK 1001 Research grants (123S582 and 123Z050), Alexander von Humboldt Research Fellowship for Experienced Researchers, Marie Skłodowska-Curie Individual Fellowship (101003361), and Royal Academy Newton-Katip Çelebi Transforming Systems Through Partnership award for financial support of this research. Opinions, interpretations, conclusions, and recommendations are those of the author and are not necessarily endorsed by the TÜBİTAK. This work was partially supported

by the Science Academy's Young Scientist Awards Program (BAGEP), Outstanding Young Scientists Awards (GEBIP), and Bilim Kahramanlari Derneği The Young Scientist Award. The authors have no other relevant affiliations or financial involvement with any organization or entity with a financial interest in or financial conflict with the subject matter or materials discussed in the manuscript apart from those disclosed. Some elements in the TOC and Figure 1 were designed using resources from Flaticon.com. We also thank Tekin Akkus for his artwork in the illustrations of Figure 1.

REFERENCES

- (1) Mishra, R.; Maiti, T. K.; Bhattacharyya, T. K. Development of SU-8 hollow microneedles on a silicon substrate with microfluidic interconnects for transdermal drug delivery. *J. Micromech. Microeng.* **2018**, *28* (10), 105017.
- (2) Parhi, R. 16—Nanocomposite for transdermal drug delivery. In *Applications of Nanocomposite Materials in Drug Delivery*; Inamuddin, A. M. A., Ed.; Woodhead Publishing, 2018; pp 353–389.
- (3) Avcil, M.; Çelik, A. Microneedles in Drug Delivery: Progress and Challenges. *Micromachines* **2021**, *12* (11), 1321.
- (4) Luo, X.; Yang, L.; Cui, Y. Microneedles: materials, fabrication, and biomedical applications. *Biomed. Microdevices* **2023**, *25* (3), 20.
- (5) Turner, J. G.; White, L. R.; Estrela, P.; Leese, H. S. Hydrogel-Forming Microneedles: Current Advancements and Future Trends. *Macromol. Biosci.* **2021**, *21* (2), No. e2000307.
- (6) Tamez-Tamez, J. I.; Vázquez-Lepe, E.; Rodriguez, C. A.; Martínez-López, J. I.; García-López, E. Assessment of geometrical dimensions and puncture feasibility of microneedles manufactured by micromilling. *Int. J. Adv. Manuf. Technol.* **2023**, *126* (11–12), 4983–4996.
- (7) Larraneta, E.; McCrudden, M. T.; Courtenay, A. J.; Donnelly, R. F. Microneedles: A New Frontier in Nanomedicine Delivery. *Pharm. Res.* **2016**, *33* (5), 1055–1073.
- (8) Gupta, J.; Felner, E. I.; Prausnitz, M. R. Minimally invasive insulin delivery in subjects with type 1 diabetes using hollow microneedles. *Diabetes Technol. Therapeut.* **2009**, *11* (6), 329–337.
- (9) Sbvj, C.; Mannayee, G. Structural analysis and simulation of solid microneedle array for vaccine delivery applications. *Mater. Today Proc.* **2022**, *65*, 3774–3779.
- (10) Aswani Kumar, G.; Rajesh Kumar, B.; Jyothi, V.; Injeti, S. Effect of Insertion Force for Successful Penetration of a Conical Shaped Microneedle into the Skin. In *Trends in Mechanical and Biomedical Design*; Akinlabi, E. T., Ramkumar, P., Selvaraj, M., Eds.; Springer: Singapore, 2021; pp 613–621.
- (11) Waghule, T.; Singhi, G.; Dubey, S. K.; Pandey, M. M.; Gupta, G.; Singh, M.; Dua, K. Microneedles: A smart approach and increasing potential for transdermal drug delivery system. *Biomed. Pharmacother.* **2019**, *109*, 1249–1258.
- (12) Ahmad, N. N.; Ghazali, N. N. N.; Wong, Y. H. Mechanical and fluidic analysis of hollow side-open and outer-grooved design of microneedles. *Mater. Today Commun.* **2021**, *29*, 102940.
- (13) Iachina, I.; Eriksson, A. H.; Bertelsen, M.; Petersson, K.; Jansson, J.; Kemp, P.; Engell, K. M.; Brewer, J. R.; Nielsen, K. T. Dissolvable microneedles for transdermal drug delivery showing skin penetration and modified drug release. *Eur. J. Pharm. Sci.* **2023**, *182*, 106371.
- (14) Lee, J. W.; Park, J. H.; Prausnitz, M. R. Dissolving microneedles for transdermal drug delivery. *Biomaterials* **2008**, *29* (13), 2113–2124.
- (15) Giri Nandagopal, M. S.; Antony, R.; Rangabhashiyam, S.; Sreekumar, N.; Selvaraju, N. Overview of microneedle system: a third generation transdermal drug delivery approach. *Microsyst. Technol.* **2014**, *20* (7), 1249–1272.
- (16) Bouwstra, J. A.; Ponc, M. The skin barrier in healthy and diseased state. *Biochim. Biophys. Acta, Biomembr.* **2006**, *1758* (12), 2080–2095.
- (17) Prausnitz, M. R. Microneedles for transdermal drug delivery. *Adv. Drug Deliv. Rev.* **2004**, *56* (5), 581–587.
- (18) Meyer, B. K.; Kendall, M. A. F.; Williams, D. M.; Bett, A. J.; Dubey, S.; Gentzel, R. C.; Casimiro, D.; Forster, A.; Corbett, H.; Crichton, M.; Baker, S. B.; Evans, R. K.; Bhambhani, A. Immune response and reactogenicity of an unadjuvanted intradermally delivered human papillomavirus vaccine using a first generation Nanopatch in rhesus macaques: An exploratory, pre-clinical feasibility assessment. *Vaccine: X* **2019**, *2*, 100030.
- (19) Reed, M.; Lye, W. K. Microsystems for drug and gene delivery. *Proc. IEEE* **2004**, *92* (1), S6–75.
- (20) Mishra, R.; Maiti, T. K.; Bhattacharyya, T. K. Design and Scalable Fabrication of Hollow SU-8 Microneedles for Transdermal Drug Delivery. *IEEE Sensor. J.* **2018**, *18* (14), S635–S644.
- (21) Tucak, A.; Sirbubalo, M.; Hindija, L.; Rahic, O.; Hadziabdic, J.; Muhamedagic, K.; Cekic, A.; Vranic, E. Microneedles: Characteristics, Materials, Production Methods and Commercial Development. *Micromachines* **2020**, *11* (11), 961.
- (22) Yan, Q.; Shen, S.; Wang, Y.; Weng, J.; Wan, A.; Yang, G.; Feng, L. The Finite Element Analysis Research on Microneedle Design Strategy and Transdermal Drug Delivery System. *Pharmaceutics* **2022**, *14*, 1625.
- (23) Makvandi, P.; Kirkby, M.; Hutton, A. R. J.; Shabani, M.; Yiu, C. K. Y.; Baghbantarahdari, Z.; Jamaledin, R.; Carlotti, M.; Mazzolai, B.; Mattoli, V.; Donnelly, R. F. Engineering Microneedle Patches for Improved Penetration: Analysis, Skin Models and Factors Affecting Needle Insertion. *Nano-Micro Lett.* **2021**, *13* (1), 93.
- (24) Milewski, M.; Stinchcomb, A. L. Vehicle composition influence on the microneedle-enhanced transdermal flux of naltrexone hydrochloride. *Pharm. Res.* **2011**, *28* (1), 124–134.
- (25) Ahmadpour, A.; Isgor, P. K.; Ural, B.; Eren, B. N.; Sarabi, M. R.; Muradoglu, M.; Tasoglu, S. Microneedle arrays integrated with microfluidic systems: Emerging applications and fluid flow modeling. *Biomicrofluidics* **2023**, *17* (2), 021501.
- (26) McAllister, D. V.; Wang, P. M.; Davis, S. P.; Park, J.-H.; Canatella, P. J.; Allen, M. G.; Prausnitz, M. R. Microfabricated needles for transdermal delivery of macromolecules and nanoparticles: Fabrication methods and transport studies. *Proc. Natl. Acad. Sci. U.S.A.* **2003**, *100* (24), 13755–13760.
- (27) Mukerjee, E. V.; Collins, S. D.; Isseroff, R. R.; Smith, R. L. Microneedle array for transdermal biological fluid extraction and in situ analysis. *Sens. Actuators, A* **2004**, *114* (2–3), 267–275.
- (28) Bodhale, D. W.; Nisar, A.; Afzulpurkar, N. Structural and microfluidic analysis of hollow side-open polymeric microneedles for transdermal drug delivery applications. *Microfluid. Nanofluidics* **2010**, *8* (3), 373–392.
- (29) Griss, P.; Stemme, G. Side-opened out-of-plane microneedles for microfluidic transdermal liquid transfer. *J. Microelectromech. Syst.* **2003**, *12* (3), 296–301.
- (30) Ingrole, R. S. J.; Gill, H. S. Microneedle Coating Methods: A Review with a Perspective. *J. Pharmacol. Exp. Ther.* **2019**, *370* (3), 555–569.
- (31) Gill, H. S.; Prausnitz, M. R. Coated microneedles for transdermal delivery. *J. Controlled Release* **2007**, *117* (2), 227–237.
- (32) Jiang, J.; Gill, H. S.; Ghate, D.; McCarey, B. E.; Patel, S. R.; Edelhauser, H. F.; Prausnitz, M. R. Coated microneedles for drug delivery to the eye. *Invest. Ophthalmol. Vis. Sci.* **2007**, *48* (9), 4038–4043.
- (33) Kim, Y. C.; Grossniklaus, H. E.; Edelhauser, H. F.; Prausnitz, M. R. Intrastromal delivery of bevacizumab using microneedles to treat corneal neovascularization. *Invest. Ophthalmol. Vis. Sci.* **2014**, *55* (11), 7376–7386.
- (34) Song, H. B.; Lee, K. J.; Seo, I. H.; Lee, J. Y.; Lee, S. M.; Kim, J. H.; Kim, J. H.; Ryu, W. Impact insertion of transfer-molded microneedle for localized and minimally invasive ocular drug delivery. *J. Controlled Release* **2015**, *209*, 272–279.
- (35) Lee, K. J.; Park, S. H.; Lee, J. Y.; Joo, H. C.; Jang, E. H.; Youn, Y. N.; Ryu, W. Perivascular biodegradable microneedle cuff for reduction of neointima formation after vascular injury. *J. Controlled Release* **2014**, *192*, 174–181.
- (36) Lee, J.; Kim, D. H.; Lee, K. J.; Seo, I. H.; Park, S. H.; Jang, E. H.; Park, Y.; Youn, Y. N.; Ryu, W. Transfer-molded wrappable microneedle meshes for perivascular drug delivery. *J. Controlled Release* **2017**, *268*, 237–246.

- (37) Ma, Y.; Boese, S. E.; Luo, Z.; Nitin, N.; Gill, H. S. Drug coated microneedles for minimally-invasive treatment of oral carcinomas: development and in vitro evaluation. *Biomed. Microdevices* **2015**, *17* (2), 44.
- (38) McNeilly, C. L.; Crichton, M. L.; Primiero, C. A.; Frazer, I. H.; Roberts, M. S.; Kendall, M. A. *Microprojection Arrays to Immunise at Mucosal Surfaces*; The Controlled Release Society, 2014; pp 1873–4995.
- (39) Lim, D. J.; Vines, J. B.; Park, H.; Lee, S. H. Microneedles: A versatile strategy for transdermal delivery of biological molecules. *Int. J. Biol. Macromol.* **2018**, *110*, 30–38.
- (40) Ita, K. Dissolving microneedles for transdermal drug delivery: Advances and challenges. *Biomed. Pharmacother.* **2017**, *93*, 1116–1127.
- (41) Rezapour Sarabi, M.; Alseed, M. M.; Karagoz, A. A.; Tasoglu, S. Machine Learning-Enabled Prediction of 3D-Printed Microneedle Features. *Biosensors* **2022**, *12* (7), 491.
- (42) Parhi, R.; Suresh, P.; Patnaik, S. Physical means of stratum corneum barrier manipulation to enhance transdermal drug delivery. *Curr. Drug Deliv.* **2015**, *12* (2), 122–138.
- (43) Akhtar, N. Microneedles: An innovative approach to transdermal delivery—a review. *Int. J. Pharm. Pharmaceut. Sci.* **2014**, *6* (4), 18–25.
- (44) Nalluri, B. N.; Anusha, S. S.; Bramhini, S. R.; Amulya, J.; Sultana, A. S.; Teja, C. U.; Das, D. B. In Vitro Skin Permeation Enhancement of Sumatriptan by Microneedle Application. *Curr. Drug Deliv.* **2015**, *12* (6), 761–769.
- (45) Verbaan, F. J.; Bal, S. M.; van den Berg, D. J.; Dijkman, J. A.; van Hecke, M.; Verpoorten, H.; van den Berg, A.; Luttege, R.; Bouwstra, J. A. Improved piercing of microneedle arrays in dermatomed human skin by an impact insertion method. *J. Controlled Release* **2008**, *128* (1), 80–88.
- (46) Loh, J. M.; Lim, Y. J. L.; Tay, J. T.; Cheng, H. M.; Tey, H. L.; Liang, K. Design and fabrication of customizable microneedles enabled by 3D printing for biomedical applications. *Bioact. Mater.* **2024**, *32*, 222–241.
- (47) Park, J. H.; Allen, M. G.; Prausnitz, M. R. Biodegradable polymer microneedles: fabrication, mechanics and transdermal drug delivery. *J. Controlled Release* **2005**, *104* (1), 51–66.
- (48) Gomaa, Y. A.; Morrow, D. I.; Garland, M. J.; Donnelly, R. F.; El-Khordagui, L. K.; Meidan, V. M. Effects of microneedle length, density, insertion time and multiple applications on human skin barrier function: assessments by transepidermal water loss. *Toxicol. In Vitro* **2010**, *24* (7), 1971–1978.
- (49) Abdullah, A. C.; Tasoglu, S. ML-Augmented Bayesian Optimization of Pain Induced by Microneedles. *Advanced Sensor Research*; Wiley, 2024; p 2300181.
- (50) Kong, X. Q.; Zhou, P.; Wu, C. W. Numerical simulation of microneedles' insertion into skin. *Comput. Methods Biomech. Biomed. Eng.* **2011**, *14* (9), 827–835.
- (51) Davis, S. P.; Landis, B. J.; Adams, Z. H.; Allen, M. G.; Prausnitz, M. R. Insertion of microneedles into skin: measurement and prediction of insertion force and needle fracture force. *J. Biomech.* **2004**, *37* (8), 1155–1163.
- (52) Mansor, N. H. A.; Markom, M. A.; Tan, E. S. M. M.; Adom, A. H. Design and Fabrication of Biodegradable Microneedle Using 3D Rapid Prototyping Printer. *J. Phys.: Conf. Ser.* **2019**, *1372*, 012053.
- (53) Aggarwal, P.; Johnston, C. R. Geometrical effects in mechanical characterizing of microneedle for biomedical applications. *Sens. Actuators, B* **2004**, *102* (2), 226–234.
- (54) Tarar, C.; Aydin, E.; Yetisen, A. K.; Tasoglu, S. Machine Learning-Enabled Optimization of Interstitial Fluid Collection via a Sweeping Microneedle Design. *ACS Omega* **2023**, *8* (23), 20968–20978.
- (55) Tarar, C.; Aydin, E.; Yetisen, A. K.; Tasoglu, S. Bayesian machine learning optimization of microneedle design for biological fluid sampling. *Sens. Diagn.* **2023**, *2* (4), 858–866.
- (56) Chiu, C.; Kuo, H.; Lin, Y.; Lee, J.-I.; Shen, Y.-K.; Kang, S. Optimal Design of Microneedles Inserts into Skin by Numerical Simulation. *Key Eng. Mater.* **2012**, *516*, 624–628.
- (57) Anbazhagan, G.; Suseela, S. B.; Sankararajan, R. Design, analysis and fabrication of solid polymer microneedle patch using CO(2) laser and polymer molding. *Drug Delivery Transl. Res.* **2023**, *13* (6), 1813–1827.
- (58) Smith, W. G. Analytic solutions for tapered column buckling. *Comput. Struct.* **1988**, *28* (5), 677–681.
- (59) Kanakaraj, U.; Lhaden, T.; Venkitaraman, K. Analysis of structural mechanics of solid microneedle using COMSOL software. *International Conference on Innovations in Information, Embedded and Communication Systems (ICIIECS)*, 2015; pp 1–5.
- (60) Fu, X.; Gu, J.; Ma, M.; Liu, R.; Bi, S.; Zhang, X.; Zhang, Y. Unique benefits and challenges of 3D-printed microneedles. *IJB* **2024**, *0* (0), 1896.
- (61) Faraji Rad, Z.; Prewett, P. D.; Davies, G. J. Rapid prototyping and customizable microneedle design: Ultra-sharp microneedle fabrication using two-photon polymerization and low-cost micromolding techniques. *Manuf. Lett.* **2021**, *30*, 39–43.
- (62) Dabbagh, S. R.; Sarabi, M. R.; Rahbarghazi, R.; Sokullu, E.; Yetisen, A. K.; Tasoglu, S. 3D-printed microneedles in biomedical applications. *Iscience* **2021**, *24* (1), 102012.
- (63) Rezapour Sarabi, M.; Nakhjavani, S. A.; Tasoglu, S. 3D-Printed Microneedles for Point-of-Care Biosensing Applications. *Micro-machines* **2022**, *13* (7), 1099.
- (64) Sarabi, M. R.; Bediz, B.; Faló, L. D.; Korkmaz, E.; Tasoglu, S. 3D Printing of Microneedle Arrays: Challenges Towards Clinical Translation. *J. 3D Print. Med.* **2021**, *5* (2), 65–70.
- (65) Sarabi, M. R.; Ahmadpour, A.; Yetisen, A. K.; Tasoglu, S. Finger-Actuated Microneedle Array for Sampling Body Fluids. *Appl. Sci.* **2021**, *11*, 5329.
- (66) Ji, H. W.; Wang, M. Y.; Wang, Y. T.; Wang, Z. H.; Ma, Y. J.; Liu, L. L.; Zhou, H. L.; Xu, Z.; Wang, X.; Chen, Y.; Feng, X. Skin-integrated, biocompatible, and stretchable silicon microneedle electrode for long-term EMG monitoring in motion scenario. *npj Flexible Electron.* **2023**, *7* (1), 46.
- (67) Vinayakumar, K. B.; Hegde, G. M.; Nayak, M. M.; Dinesh, N. S.; Rajanna, K. Fabrication and characterization of gold coated hollow silicon microneedle array for drug delivery. *Microelectron. Eng.* **2014**, *128*, 12–18.